

Strain Anisotropy and Magnetic Domains in Embedded Nanomagnets

Magnus Nord,* Anna Semisalova, Attila Kákay, Gregor Hlawacek, Ian MacLaren,* Vico Liersch, Oleksii M. Volkov, Denys Makarov, Gary W. Paterson, Kay Potzger, Jürgen Lindner, Jürgen Fassbender, Damien McGrouther, and Rantej Bali*

Nanoscale modifications of strain and magnetic anisotropy can open pathways to engineering magnetic domains for device applications. A periodic magnetic domain structure can be stabilized in sub-200 nm wide linear as well as curved magnets, embedded within a flat non-ferromagnetic thin film. The nanomagnets are produced within a non-ferromagnetic B2-ordered Fe₆₀Al₄₀ thin film, where local irradiation by a focused ion beam causes the formation of disordered and strongly ferromagnetic regions of A2 Fe₆₀Al₄₀. An anisotropic lattice relaxation is observed, such that the in-plane lattice parameter is larger when measured parallel to the magnet short-axis as compared to its length. This in-plane structural anisotropy manifests a magnetic anisotropy contribution, generating an easy-axis parallel to the short axis. The competing effect of the strain and shape anisotropies stabilizes a periodic domain pattern in linear as well as spiral nanomagnets, providing a versatile and geometrically controllable path to engineering the strain and thereby the magnetic anisotropy at the nanoscale.

1. Introduction

Magnetic domains form the core of a variety of data storage concepts,^[1–5] as well as sensing devices.^[6,7] Most of these devices require that the magnetic domains formed within nanostructured regions are stable, such that a reference domain configuration can be restored after the application and release of external stimulus such as magnetic fields and spin-currents. The local alignment of magnetic moments can be converted to an electrical signal via magnetoresistance effects, and any change to the domain structure against the reference is read as the signal.

The requirement of achieving stable magnetic domains at the nanoscale has driven a large volume of research, and a variety of approaches have been deployed.^[8–23] The simplest path is to produce high-aspect

ratio magnetic structures, where the magnetostatic fields force moments to align along an axis dictated by the overall shape. Magnetostatic effects induced by shape alone tend to be weak and are sensitive to stochastic domain formation due to microscopic structural defects and surface roughness. Multidomain structures can be realized in the presence of two or more preferential axes for moment alignment. Preferential anisotropy axes can be induced in a variety of ways, for instance by directional annealing in applied magnetic fields, nanoscale surface modulations, and exchange coupling by interfacing with anti-ferromagnets, all of which allow a degree of control over the domain structure, but are susceptible to variations in the process conditions.


A more reliable path is to structurally modify the material, for instance, the magneto-crystalline anisotropy can be modified via lattice distortions, thereby inducing preferential lattice-driven axes for moment alignment.^[11–13] Lattice distortions can be induced, for instance, in films grown on single crystals with mismatched lattice parameters, or on piezoelectric substrates.^[14–17] The axes along which lattice distortions can be realized are restricted by the substrate crystallography, and inducing strains in curved structures can be challenging in practice. Where two competing anisotropies are induced, each corresponding to easy axes oriented perpendicular to each other, a periodic magnetic domain structure is theoretically predicted.^[18,19] The periodicity of the domains is determined by the relative magnitudes of the anisotropy energies, imparting a degree of control over the periodicity. Experimentally,

Dr. M. Nord, Dr. I. MacLaren, Dr. G. W. Paterson, Dr. D. McGrouther
SUPA

School of Physics and Astronomy
University of Glasgow
Glasgow G12 8QQ, UK
E-mail: Ian.MacLaren@glasgow.ac.uk

Dr. M. Nord
Electron Microscopy for Materials Science
University of Antwerp
Antwerp 2000, Belgium
E-mail: magnus.nord@uantwerpen.be

Dr. A. Semisalova,^[†] Dr. A. Kákay, Dr. G. Hlawacek, V. Liersch,
Dr. O. M. Volkov, Dr. D. Makarov, Dr. K. Potzger, Dr. J. Lindner,
Prof. J. Fassbender, Dr. R. Bali
Institute of Ion Beam Physics and Materials Research
Helmholtz-Zentrum Dresden-Rossendorf
01328 Dresden, Germany
E-mail: r.bali@hzdr.de

 The ORCID identification number(s) for the author(s) of this article can be found under <https://doi.org/10.1002/smll.201904738>.

© 2019 The Authors. Published by WILEY-VCH Verlag GmbH & Co. KGaA, Weinheim. This is an open access article under the terms of the Creative Commons Attribution License, which permits use, distribution and reproduction in any medium, provided the original work is properly cited.

^[†]Present address: Faculty of Physics, University of Duisburg-Essen, Duisburg, Germany

DOI: 10.1002/smll.201904738

such periodic domains have been observed in micrometer-sized magnetic structures.^[24–27]

Magnetism in curved geometries is an emergent field where curvature-driven magneto-chiral effects may open new applications in domain wall devices.^[28] Engineering magnetic anisotropies in curved nanomagnets through strain is however challenging, since most methods rely on linear strains.

Here, we consider the case magnetic domains within nanomagnets generated in an ordered alloy thin film by localized chemical disordering. We show that periodic magnetic domains can be stabilized in embedded nanomagnets of linear as well as curved geometries. An in-plane lattice distortion coincides with the occurrence of domain periodicity. Micromagnetic simulations show that the domain periodicity is consistent with the occurrence of a large uniaxial magnetic anisotropy, K_U , such that an easy axis is generated parallel to the narrow dimension of the nanomagnets.

A prototype material for producing embedded nanomagnets embedded is B2 $\text{Fe}_{60}\text{Al}_{40}$.^[29–38] The B2 ordered alloy acts as a non-ferromagnetic template, which can be irradiated using ion- or laser- beams to generate local disordering.^[29,38] Disorder of the Fe and Al-rich 100 planes leads to antisite defects and the formation of A2 $\text{Fe}_{60}\text{Al}_{40}$, which is ferromagnetic, possessing a saturation magnetization (M_s) of up to $\approx 800 \text{ kA m}^{-1}$.^[29] Focused ion- and laser- beams can therefore be used to locally embed nanomagnets at desired locations, and also induce a nanoscale modification of the in-plane lattice parameter.

Linear magnetic stripes were generated by ion bombardment using a highly focused Ne^+ -beam of $\approx 2 \text{ nm}$ diameter from a gas field ion source.^[39] Within the non-ferromagnetic B2 $\text{Fe}_{60}\text{Al}_{40}$ structure penetrating ions undergo knock-on collisions with the host Fe (Al) atoms, forming vacancies which stochastically recombine with thermally diffusing Al (Fe) atoms, resulting in antisite defects. Antisite disorder, formed by site-swapping between the Fe and Al atoms, leads to an increase in the Fe–Fe exchange interaction and the onset of ferromagnetism. Variations of the local densities of states at the antisites may also result in a lattice expansion, which can contribute to the increase of M_s . An easy-plane anisotropy has been shown to occur in continuous films of A2 $\text{Fe}_{60}\text{Al}_{40}$, where the anisotropy is isotropic in-plane and is related to the lattice relaxation due to increasing thickness.^[40] Here we show that the easy-plane anisotropy observed in continuous films is broken by the lattice distortion emergent from the high aspect ratio geometry of the objects investigated in this study.

2. Results

Linear magnetic stripes of width, $w = 30, 195, 235, 295, 410,$ and $660 \text{ nm}, 1.1, 2.1,$ and $4 \mu\text{m}$ (error $\pm 10 \text{ nm}$) with fixed length, l of $10 \mu\text{m}$ were prepared by disordering locally confined regions of 40 nm thick B2 $\text{Fe}_{60}\text{Al}_{40}$ template films with the Ne^+ ion

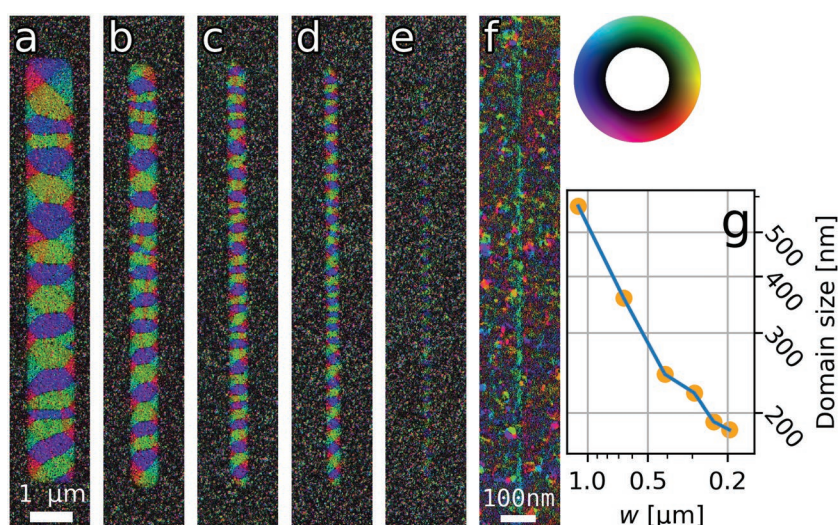


Figure 1. STEM-DPC images of magnetic stripes. Magnetic domain structure for stripes with width, w of a) $1.1 \mu\text{m}$, b) 660 nm , c) 410 nm , d) 295 nm , e) 195 nm , f) 30 nm . Domain size measured along the length, as a function of stripe width is shown in g). The color code indicating moment direction in (a–f) is shown on the top right.

beam. Control structures possessing curvature viz., magnetic disc of $4 \mu\text{m}$ diameter, as well as an archimedean spiral with a curving arm of 500 nm width and the same interarm spacing were also produced. The Ne^+ -energy and fluence were kept fixed at 26 keV and 6 ions nm^{-2} respectively, in order to achieve a homogeneous M_s within the 40 nm film thickness, known from previous observations on continuous thin film samples.^[41] The films were prepared on 20 nm thick Si-N membranes to enable scanning transmission electron microscopy with a fast pixelated detector (4D-STEM) in order to simultaneously resolve both structural and magnetic domain structure.

Differential phase contrast (DPC)^[42] images determined from the deflection of the beam as a function of position showed well-defined periodic domain structure in stripes with $2 \mu\text{m} < w < 30 \text{ nm}$ (Figure 1a–f). The domains in wider stripes (not shown) are irregular, as the stripe approaches the continuous thin film limit. Conversely, the narrowest stripe with $w = 30 \text{ nm}$ (Figure 1f) only shows a y -component along the length (see Figure S3 in the Supporting Information). The periodicity shows a monotonic decrease with w (Figure 1g). As seen in Figure 1g, the stripe with $w = 1.1 \mu\text{m}$ possesses a domain periodicity of 570 nm , whereas in the narrow stripes where $w < 660 \text{ nm}$, the periodicity tends toward w , with periodicities of 191 and 183 nm for $w = 235$ and 195 nm respectively.

The lattice parameter, a_0 , corresponding to the above-seen domain structures can be directly measured by summing subsets of the same scanned diffraction datasets used to resolve the magnetic domain structure, by measuring the diameter of the polycrystalline 110 ring in the diffraction patterns, shown in Figure 2a. The inset of Figure 2a shows that, by direct visual inspection, the ring radius of the irradiated (A2) and nonirradiated (B2) regions (arrows) is different, with the patterned regions possessing a larger lattice parameter (inversely proportional to the ring radius). Summing the patterns along the length of the stripe, gives diffraction patterns (as seen in Figure 2a) as a function of position across the width of the

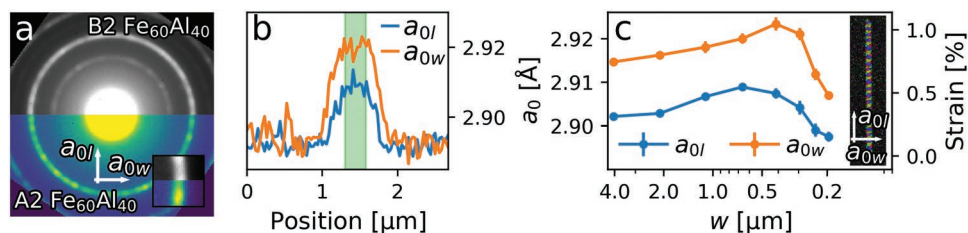


Figure 2. In-plane lattice parameter estimation. a) Sum of several STEM diffraction images, leading to averaged STEM diffraction images from patterned and nonpatterned regions in stripes with $w = 1.1 \mu\text{m}$, showing difference in lattice sizes parallel to the w -axis (a_{0w}); the bright diffracted ring is the 110 ring for the cubic structure. b) Anisotropic lattice parameter of the $w = 660 \text{ nm}$ stripe, across the width of the stripe. c) The variations of a_{0w} and a_{0l} as a function of w . The lattice parameters were averaged over the shaded region shown in (b). The definition of a_{0w} and a_{0l} is described in the inset.

stripe. Ellipses are fitted to the 110 $\text{Fe}_{60}\text{Al}_{40}$ diffraction ring for each of these diffraction patterns, resulting in a measurement of a_0 as function of the position across each stripe (Figure 2b–c). Account was taken of the slight intrinsic level of elliptical distortion arising from the microscope’s electron optics by measuring the nonpatterned region. It can be observed that within the each stripe, there occur significant differences between the in-plane lattice parameters measured along the l - and w -axis viz., a_{0l} and a_{0w} respectively. The differences in a_{0l} and a_{0w} for $w = 660 \text{ nm}$ are shown in Figure 2b, where $a_{0w} > a_{0l}$ across the stripe width.

3. Discussion

The estimated values of a_{0w} and a_{0l} , are plotted in Figure 2c, as a function of w . It can be observed that $a_{0w} > a_{0l}$ over the measured w -range. A variation of a_{0w} and a_{0l} with increasing w is also observed; both the lattice parameters increase sharply up to $w = 660 \text{ nm}$, followed by a gradual decrease in a_0 with a further increase in w . Even for the widest stripes considered viz., $w = 4 \mu\text{m}$, the in-plane lattice anisotropy is preserved.

Micromagnetic simulations were performed to estimate the conditions under which the periodic domains can be formed in the investigated structures. Magnetic stripes of $l = 10 \mu\text{m}$ in length, $w = 30, 250, \text{ and } 500 \text{ nm}$ in width were considered. Material parameters of the ferromagnetic $\text{Fe}_{60}\text{Al}_{40}$ were used: saturation magnetization $M_s = 790 \text{ kA m}^{-1}$ and exchange stiffness $A = 4.1 \text{ pJ m}^{-1}$.^[29,37] To produce the periodic domains it was necessary to include a uniaxial anisotropy, K_U , with its easy-axis oriented perpendicular to the l -axis. The equilibrium domain configurations for the nanowires with different width were calculated using anisotropy values K_U between 0 and 10^4 J m^{-3} . As shown in Figure 3a–e), the assumption of K_U allows the periodic domains to be reproduced in stripes with $w = 1 \mu\text{m}$ down to 195 nm. For every w , the K_U was varied, and the minimum K_U that is necessary to simulate the periodic domains are shown in Figure 3f).

To check the possibility to introduce strain-induced anisotropy into the curvilinear geometries, Archimedean spirals with a curving arm of 500 and 500 nm interarm spacing was patterned. The focused Ne^+ -ion beam was rastered in the same manner as for the linear stripes, i.e., along the x -axis with beam-blanking in regions not to be irradiated. STEM-DPC

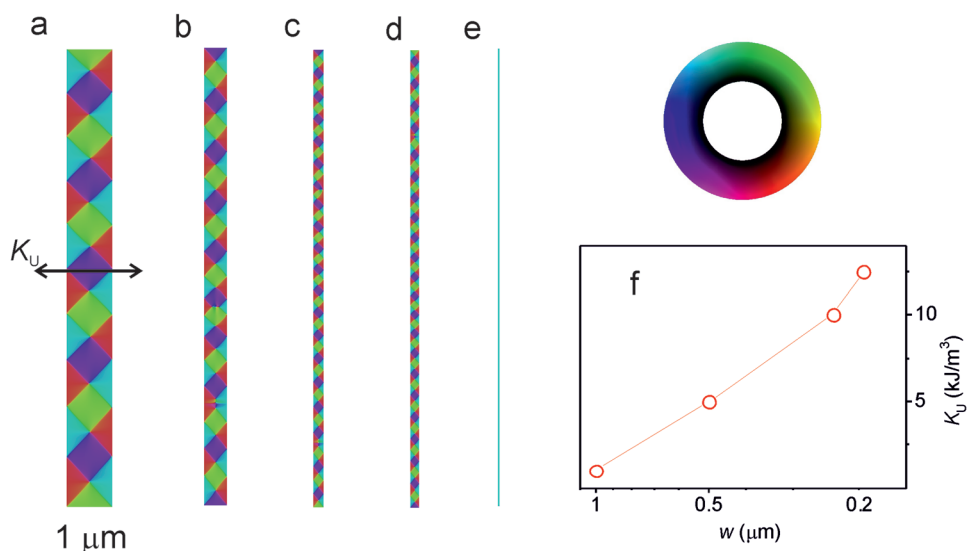


Figure 3. Micromagnetic simulations of stripe structures. Simulated magnetic domain structure for stripes with width w of a) $1 \mu\text{m}$, b) 500 nm , c) 235 nm , d) 195 nm , and e) 30 nm . f) The minimum uniaxial anisotropy constant, K_U , that is necessary to induce the domain structure, as obtained from simulations. Color code indicating moment direction in (a–e) is shown on the top right. Arrows indicate the orientation of the anisotropy axis in (a–e).

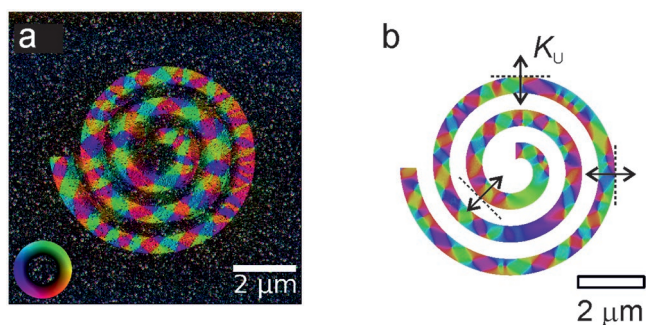


Figure 4. Magnetic domain formation in a spiral structure. a) STEM-DPC image of the magnetic domains and b) micromagnetic simulation of the structure. K_U is the uniaxial anisotropy considered in the simulation. Arrows in b) indicate the orientation of the local anisotropy axes.

images show that similar to the case of linear stripes, domain periodicity also tends to occur in the spiral structure (Figure 4a). A large domain inconsistent with the periodicity is observed on the outermost arm; nevertheless domain periodicity largely persists in a majority of the structure.

The domain periodicity can be reproduced in simulations (Figure 4b) when a uniaxial anisotropy with its easy axis always oriented radial to the curvature is assumed. The magnitude of the anisotropy in Figure 4b is assumed to be the same as that for 500 nm wide linear stripes ($K_U = 5 \text{ kJ m}^{-3}$). Running the simulation in the absence of K_U gives a single domain spiral structure. The necessity to introduce K_U to reproduce the experimentally observed domain periodicity suggests that the in-plane lattice distortion is also present in the curved structure, and instead of the l and w axes for linear stripes, the distortion occurs along the tangential and radial axes, respectively.

The occurrence of in-plane strain anisotropy in embedded nanomagnets implies that there must exist corresponding in-plane inhomogeneous strain fields. Bulk, fully ferromagnetic A2 $\text{Fe}_{60}\text{Al}_{40}$ is known to possess an $a_0 \approx 2.93 \text{ \AA}$, which is 1.4% larger than that of the B2 phase with $a_0 \approx 2.89 \text{ \AA}$.^[43] In Figure 2d, the a_0 of embedded A2 $\text{Fe}_{60}\text{Al}_{40}$ nanomagnets varies in the range 2.90–2.92 \AA . These values are smaller than expected for A2 $\text{Fe}_{60}\text{Al}_{40}$. Thus the magnetic regions are constrained by the surrounding B2 structured film, inducing a compressive strain. From Figure 2 we also note that the lattice parameters along the w -axis of the linear stripe exhibit values which are 1.036–1.042 times larger than those along the l -axis suggesting that the corresponding strain field is inhomogeneous and there is greatest compressive strain along the l -axis.

Irradiation of the B2 structured film leads to the creation of atomic scale chemical disorder through the formation of vacancies, interstitials and other defects. Associated with the generation of chemical disorder is the increase in the lattice parameter.^[44,45] However, because the A2 $\text{Fe}_{60}\text{Al}_{40}$ regions are bound by a vastly greater expanse of B2 $\text{Fe}_{60}\text{Al}_{40}$, free expansion is constrained and an enlarged lattice parameter is only accommodated through the occurrence of a degree of distortion, such as by z -axis expansion or bowing of the film, allowed by the mechanical properties of the film and substrate. We observe

here that in embedded A2 $\text{Fe}_{60}\text{Al}_{40}$ regions, relaxation occurs via an anisotropic lattice distortion.

The above discussion addresses the direct mechanical effects associated with definition of the structures. It is likely that the overall strain relaxation also involves an atomic scale structural response. Anisotropic strain relaxation leading to uniaxial anisotropy has been reported in epitaxial films grown on single crystal substrates, where the anisotropic relaxation occurs due to surface reconstructions, or dislocations that break crystal symmetry.^[46,47] In polycrystalline films, lattice distortion in the perpendicular to plane direction has been attributed to the generation of vacancies at the free surface and their diffusion toward grain boundaries.^[48] In structures embedded within polycrystalline films, the latter, vacancy mediated mechanism is likely to play an important role in strain relaxation as well. $\text{Fe}_{60}\text{Al}_{40}$ is known to possess a high equilibrium vacancy concentration, which can mediate diffusion during the irradiation process.^[49,50]

4. Conclusion

In conclusion, nanostructures embedded within polycrystalline alloy thin films can show a structural relaxation that is anisotropic within the film plane and dependent on the nanostructure geometry. The in-plane structural anisotropy that follows geometric curvature opens a pathway to engineering strain as well as the functional properties that manifest from it at the nanoscale. In high-aspect ratio A2 $\text{Fe}_{60}\text{Al}_{40}$ embedded within B2 $\text{Fe}_{60}\text{Al}_{40}$ films, the anisotropic strain leads to a uniaxial anisotropy such that a periodic domain structure is stabilized within sub-200 nm width linear stripes, as well as in curved objects. The observed anisotropic strain can be a crucial consideration in understanding the properties of embedded nanostructures for controlling the magnetic domain structure and structure dependent properties.

5. Experimental Section

Differential Phase Contrast Imaging: The STEM data was acquired using a probe aberration corrected JEOL ARM200cF equipped with a Merlin for EM (Medipix3) fast pixelated detector from Quantum Detectors Ltd. (Harwell, UK). The TEM was operated with the objective lens turned off to allow for imaging in field-free Lorentz mode, while retaining a spatial resolution of 2.6 nm.^[51] Data was acquired using pixelated STEM (4D-STEM), where a convergent beam low angle diffraction pattern was acquired for every probe position in the raster scan. This diffraction pattern included both the direct beam which was used to determine the magnetic domain structure through STEM-DPC,^[42,52] and the (110) diffraction spots (seen as rings in Figure 2a) which was used for the structural analysis.^[53] A convergence semi angle of 0.58 mrad was used to increase the magnetic sensitivity, as well as to reduce overlap between diffraction discs for the structural analysis.

STEM-DPC allows for quantitative characterization of the in-plane magnetic induction. Changes in the in-plane magnetic induction leads to a shift of the electron beam due to the Aharonov–Bohm effect,^[42] which was measured using the phase correlation functionality in the *fpd* Python library.^[54] Using phase correlation reduces the effects of diffraction and structural contrast, which varies greatly in this sample due to its nanocrystallinity. The effects of impure scan shift (mixing of beam shift and tilt) was corrected by fitting a 2D-polynomial to the

shifts determined in the paramagnetic region, interpolating across the stripe, and subtracting this from the entire dataset. Domain width was calculated by using the magnitude of the x-component of the magnetic induction (Figure S1, Supporting Information), and the width of the stripes themselves was calculated using the total shift magnitude (Figure 2, Supporting Information).

Structural Analysis: The structural analysis was performed by using the 110 Fe₆₀Al₄₀ diffraction ring. The grains in the Fe₆₀Al₄₀ film were much smaller than the size of the stripes, and the orientation of these grains were random. However, the probe size was such that only few grains were sampled per probe position. This means that even if diffraction patterns were acquired for every probe position, the lattice size cannot be determined with sufficient accuracy for each probe position. Only a fraction of the grains will have the correct orientation to produce diffraction patterns with usable information about the lattice size (i.e., a 110 diffraction spot). By summing several single diffraction patterns (Figure S4, Supporting Information), the lattice size can be determined. This reduces the spatial resolution. However, by only averaging along the length of the stripe, the lattice size in both directions as a function of position across the width of the stripe can be determined. The angular difference between the real space image and the diffraction pattern was determined by using the direction of the magnetization in magnetic domains in the stripe as a calibration. This rotation was applied to both Figure 2a and Figure S4b in the Supporting Information, leading to the zero values in the corners. The 110 diffraction rings seen in Figure 2a and Figure S4 in the Supporting Information are radially integrated along angular slices from the center, followed by subtraction of the monotonically decreasing background similarly to the processing in Nord et al.,^[55] then a Gaussian was fitted to the remaining peak. This process results in the summed 110 diffraction ring, which can be fitted with an ellipse, yielding the lattice parameters along the length (*l*) and the width (*w*) directions. The nonirradiated region was used as a reference for the lattice parameter. All structural analysis data processing was done using pixStem,^[56] which relies on HyperSpy.^[57]

Micromagnetic Simulations: Micromagnetic simulations were performed using the open source GPU-accelerated finite difference code, MuMax³,^[58] and a GPU-accelerated in-house developed finite element micromagnetic code, the successor of the TetraMag.^[59,60] The material parameters in the simulations were chosen such to mimic the ferromagnetic Fe₆₀Al₄₀ alloy, namely saturation magnetization $M_s = 790 \text{ kA m}^{-1}$ and exchange stiffness $A = 4.1 \text{ pJ m}^{-1}$. To mimic the strain induced anisotropy a uniaxial anisotropy was assumed, with an easy axis perpendicular to the long axis and with an anisotropy value K_U ranging between 0 and $10\,000 \text{ J m}^{-3}$. Magnetic straight stripes of $l = 10 \text{ }\mu\text{m}$ in length, $w = 30, 250, \text{ and } 500 \text{ nm}$ in width as well as an Archimedean spiral with 500 nm arm width and 500 nm spacer with radial anisotropy were considered in the simulations. The equilibrium domain configuration was calculated for the wires with different width and varying anisotropy constant to have an estimate of the anisotropy values required to form the periodical domain pattern.

Supporting Information

Supporting Information is available from the Wiley Online Library or from the author.

Acknowledgements

Financial support from the Deutsche Forschungsgemeinschaft (DFG) through the Grants No. BA5656/1-1 and EPSRC via the project “Fast Pixel Detectors: a paradigm shift in STEM imaging” (Grant reference EP/M009963/1) is acknowledged. Irradiation experiments were performed at the Ion Beam Center of the Helmholtz-Zentrum Dresden-Rossendorf (HZDR). Caleb MacLaren assisted with the DPC image calculations.

Conflict of Interest

The authors declare no conflict of interest.

Keywords

curved magnets, embedded nanomagnets, ion-induced patterning, magnetic domains, strain anisotropy

Received: August 22, 2019

Revised: September 27, 2019

Published online:

- [1] S. S. P. Parkin, M. Hayashi, L. Thomas, *Science* **2008**, *320*, 190.
- [2] K. Chesnel, in *Magnetism and Magnetic Materials* (Ed: N. Panwar), IntechOpen, London **2017**, Ch. 3.
- [3] J. H. Franken, H. J. M. Swagten, B. Koopmans, *Nat. Nanotechnol.* **2012**, *7*, 499.
- [4] L. O'Brien, D. E. Read, H. T. Zeng, E. R. Lewis, D. Petit, R. P. Cowburn, *Appl. Phys. Lett.* **2009**, *95*, 232502.
- [5] A. Hubert, R. Schäfer, *Magnetic Domains*, Springer-Verlag, Berlin **1998**.
- [6] M. Jovičević Klug, L. Thormählen, V. Rößisch, S. D. Toxværd, M. Höft, R. Knöchel, E. Quandt, D. Meyners, J. McCord, *Appl. Phys. Lett.* **2019**, *114*, 192410.
- [7] J. McCord, *J. Phys. D: Appl. Phys.* **2015**, *48*, 333001.
- [8] R. Bali, H. Marchetto, A. Barcza, M. G. Blamire, S. S. Dhesi, *Appl. Phys. Lett.* **2012**, *101*, 052403.
- [9] R. Bali, B. B. Nelson-Cheeseman, A. Scholl, E. Arenholz, Y. Suzuki, M. G. Blamire, *J. Appl. Phys.* **2009**, *106*, 113925.
- [10] R. Bali, N. A. Stelmashenko, M. G. Blamire, *J. Appl. Phys.* **2008**, *103*, 053911.
- [11] K.-W. Lin, C. Ouyang, J. van Lierop, in *Solid State Physics* (Eds: R. Stamps, B. Camley), Elsevier, Netherlands **2018**, Ch. 1.
- [12] D. Sander, *J. Phys.: Condens. Matter* **2004**, *16*, R603.
- [13] M. Urbánek, L. Flajšman, V. Křižáková, J. Gloss, M. Horký, M. Schmid, P. Varga, *APL Mater.* **2018**, *6*, 060701.
- [14] T. Saerbeck, J. de la Venta, S. Wang, J. G. Ramírez, M. Erekhinsky, Valmianski, I. K. Schuller, *J. Mater. Res.* **2014**, *29*, 2353.
- [15] J.-M. Hu, C. W. Nan, *Phys. Rev. B* **2009**, *80*, 224416.
- [16] J.-M. Hu, Z. Li, L.-Q. Chen, C. W. Nan, *Adv. Mater.* **2012**, *24*, 21.
- [17] K. Y. Wang, A. W. Rushforth, V. A. Grant, R. P. Campion, K. W. Edmonds, C. R. Staddon, C. T. Foxon, B. L. Gallagher, *J. Appl. Phys.* **2007**, *101*, 106101.
- [18] C. Kittel, *Phys. Rev.* **1946**, *70*, 965.
- [19] F. Viot, L. Favre, R. Hayn, M. D. Kuz'min, *J. Phys. D: Appl. Phys.* **2012**, *45*, 405003.
- [20] S.-H. Huang, C.-H. Lai, *Appl. Phys. Lett.* **2009**, *95*, 032505.
- [21] E. Berganza, C. Bran, M. Jaafar, M. Vázquez, A. Asenjo, *Sci. Rep.* **2016**, *6*, 29702.
- [22] T. Jin, D. Kumar, W. Gan, M. Ranjbar, F. Luo, R. Sbiaa, X. Liu, W. S. Lew, S. N. Piramanayagam, *Phys. Status Solidi RRL* **2018**, *12*, 1800197.
- [23] M. Al Bahri, B. Borie, T. L. Jin, R. Sbiaa, M. Kläui, S. N. Piramanayagam, *Phys. Rev. Appl.* **2019**, *11*, 024023.
- [24] J. Steiner, R. Schäfer, H. Wiczorek, J. McCord, F. Otto, *Phys. Rev. B* **2012**, *85*, 104407.
- [25] A. Biehler, M. Kläui, M. Fonin, C. König, G. Güntherodt, U. Rüdiger, *Phys. Rev. B* **2007**, *75*, 184427.
- [26] K. Gross, P. Szary, O. Petravic, F. Brüßing, K. Westerholt, H. Zabel, *Phys. Rev. B* **2011**, *84*, 054456.
- [27] R. D. Gomez, T. V. Luu, A. O. Pak, K. J. Kirk, J. N. Chapman, *J. Appl. Phys.* **1999**, *85*, 6163.

- [28] R. Streubel, P. Fischer, F. Kronast, V. P. Kravchuk, D. D. Sheka, Y. Gaididei, O. G. Schmidt, D. Makarov, *J. Phys. D: Appl. Phys.* **2016**, *49*, 363001.
- [29] R. Bali, S. Wintz, F. Meutzner, R. Hübner, R. Boucher, A. A. Ünal, S. Valencia, A. Neudert, K. Potzger, J. Bauch, F. Kronast, S. Facsko, J. Lindner, J. Fassbender, *Nano Lett.* **2014**, *14*, 435.
- [30] A. J. Bradley, A. H. Jay, *Proc. R. Soc. London, Ser. A* **1932**, *136*, 210.
- [31] P. A. Beck, *Metall. Mater. Trans. B* **1971**, *2*, 2015.
- [32] J. Fassbender, M. O. Liedke, T. Strache, W. Möller, E. Menendez, J. Sort, K. V. Rao, S. C. Deevi, J. Nogues, *Phys. Rev. B* **2008**, *77*, 174430.
- [33] J. Sort, A. Concustell, E. Menéndez, S. Suriñach, K.V. Rao, S. C. Deevi, M. D. Baró, J. Nogué, *Adv. Mater.* **2006**, *18*, 1717.
- [34] E. Menéndez, M. O. Liedke, J. Fassbender, T. Gemming, A. Weber, L. J. Heyderman, K. V. Rao, S. C. Deevi, S. Suriñach, M. D. Baró, J. Sort, J. Nogué, *Small* **2009**, *5*, 229.
- [35] M. Krupinski, R. Bali, D. Mitin, P. Sobieszczyk, J. Gregor-Pawlowski, A. Zarzycki, R. Böttger, M. Albrecht, K. Potzger, M. Marszałek, *Nanoscale* **2019**, *11*, 8930.
- [36] F. Röder, G. Hlawacek, S. Wintz, R. Hübner, L. Bischoff, H. Lichte, K. Potzger, J. Lindner, J. Fassbender, R. Bali, *Sci. Rep.* **2015**, *5*, 16786.
- [37] N. Tahir, R. Bali, R. Gieniusz, S. Mamica, J. Gollwitzer, T. Schneider, K. Lenz, K. Potzger, J. Lindner, M. Krawczyk, J. Fassbender, A. Maziewski, *Phys. Rev. B* **2015**, *92*, 144429.
- [38] J. Ehrler, M. He, M. V. Shugaev, N. I. Polushkin, S. Wintz, V. Liersch, S. Cornelius, R. Hübner, K. Potzger, J. Lindner, J. Fassbender, A. A. Ünal, S. Valencia, F. Kronast, L. V. Zhigilei, R. Bali, *ACS Appl. Mater. Interfaces* **2018**, *10*, 15232.
- [39] G. Hlawacek, V. Veligura, R. van Gastel, B. Poelsema, *J. Vac. Sci. Technol., B: Nanotechnol. Microelectron.: Mater., Process., Meas., Phenom.* **2014**, *32*, 020801.
- [40] T. Schneider, K. Lenz, A. S. Semisalova, J. Gollwitzer, J. Heitler-Klevans, K. Potzger, J. Fassbender, J. Lindner, R. Bali, *J. Appl. Phys.* **2019**, *125*, 19.
- [41] S. A. Cybart, R. Bali, G. Hlawacek, F. Röder, J. Fassbender, in *Helium Ion Microscopy* (Eds: G. Hlawacek, A. Götzhauser), Springer International Publishing, Switzerland **2016**, pp. 415–445.
- [42] J. N. Chapman, I. R. McFadyen, S. McVitie, *IEEE Trans. Magn.* **1990**, *26*, 1506.
- [43] E. Menéndez, J. Sort, M. O. Liedke, J. Fassbender, S. Suriñach, M. D. Baró, J. Nogué, *New J. Phys.* **2008**, *10*, 103030.
- [44] S. Gialanella, X. Amils, M. Baró, P. Delcroix, G. L. Car, L. Lutterotti, S. Suriñach, *Acta Mater.* **1998**, *46*, 3305.
- [45] M. Fujii, K. Saito, K. Wakayama, M. Kawasaki, T. Yoshioka, T. Isshiki, K. Nishio, M. Shiojir, *Philos. Mag. A* **1999**, *79*, 2013.
- [46] Y. B. Xu, D. J. Freeland, M. Tselepi, J. A. C. Bland, *Phys. Rev. B* **2000**, *62*, 1167.
- [47] O. Thomas, Q. Shen, P. Schieffer, N. Tournerie, B. Lépine, *Phys. Rev. Lett.* **2003**, *90*, 017205.
- [48] W. Gruber, S. Chakravarty, C. Baetz, W. Leitenberger, M. Bruns, A. Kobler, C. Kübel, H. Schmidt, *Phys. Rev. Lett.* **2011**, *107*, 265501.
- [49] M. O. Liedke, W. Anwand, R. Bali, S. Cornelius, S. Butterling, T. T. Trinh, A. Wagner, S. Salamon, D. Walecki, A. Smekhova, H. Wende, K. Potzger, *J. Appl. Phys.* **2015**, *117*, 163908.
- [50] J. Ehrler, M. O. Liedke, J. Čížek, R. Boucher, M. Butterling, S. Zhou, R. Böttger, E. Hirschmann, T. T. Trinh, A. Wagner, J. Lindner, J. Fassbender, C. Leyens, K. Potzger, R. Bali, *Acta Mater.* **2019**, *176*, 167.
- [51] S. McVitie, D. McGrouther, S. McFadzean, D. A. MacLaren, K. J. O'Shea, M. J. Benitez, *Ultramicroscopy* **2015**, *152*, 57.
- [52] M. Krajinak, D. McGrouther, D. Maneuski, V. O'Shea, S. McVitie, *Ultramicroscopy* **2016**, *165*, 42.
- [53] A. Béché, J. L. Rouvière, L. Clément, J. M. Hartmann, *Appl. Phys. Lett.* **2009**, *95*, 123114.
- [54] FPD: Fast pixelated detector data storage, analysis and visualization, <https://gitlab.com/fpdpy/fpd> (accessed: August 2019).
- [55] M. Nord, A. Ross, D. McGrouther, J. Barthel, M. Moreau, I. Hallsteinsen, T. Tybell, I. MacLaren, *Phys. Rev. Mater.* **2019**, *3*, 063605.
- [56] pixStem: Analysis of pixelated STEM data, <https://pixstem.org/> (accessed: August 2019).
- [57] F. de la Peña, V. T. Fauske, P. Burdet, E. Prestat, P. Jokubauskas, M. Nord, T. Ostasevicius, K. E. MacArthur, M. Sarahan, D. N. Johnstone, J. Taillon, A. Eljarrat, V. Migunov, J. Caron, T. Furnival, S. Mazzucco, T. Aarholt, M. Walls, T. Slater, F. Winkler, B. Martineau, G. Donval, R. McLeod, E. R. Hoglund, I. Alxneit, I. Hjorth, T. Henninen, L. F. Zagonel, A. Garmannslund, A. Skorikov, *hyperspy/hyperspy v1.4.1*, **2018**, <https://doi.org/10.5281/zenodo.1469364>.
- [58] A. Vansteenkiste, J. Leliaert, M. Dvornik, M. Helsen, F. Garcia-Sanchez, B. Van Waeyenberge, *AIP Adv.* **2014**, *4*, 107133.
- [59] R. Hertel, in *Handbook of Magnetism and Advanced Magnetic Materials* (Eds: H. Kronmüller, S. Parkin), John Wiley & Sons, New York **2007**.
- [60] A. Kákay, E. Westphal, R. Hertel, *IEEE Trans. Magn.* **2010**, *46*, 2303.